Short Papers

Optimization of a Parallel Shoulder Mechanism to Achieve a High-Force, Low-Mass, Robotic-Arm Exoskeleton

Julius Klein, *Member, IEEE*, Steve Spencer, *Student Member, IEEE*, J. Allington, James E. Bobrow, *Member, IEEE*, and David J. Reinkensmeyer, *Member, IEEE*

Abstract—This paper describes a robotic-arm exoskeleton that uses a parallel mechanism inspired by the human forearm to allow naturalistic shoulder movements. The mechanism can produce large forces through a substantial portion of the range of motion (RoM) of the human arm while remaining lightweight. This paper describes the optimization of the exoskeleton's torque capabilities by the modification of the key geometric design parameters.

Index Terms—Arm exoskeleton, parallel mechanism, pneumatic robot, rehabilitation devices.

I. INTRODUCTION

The development of a light and powerful robotic-arm exoskeleton is an important goal for the field of robot-assisted movement training, as well as virtual reality systems that incorporate haptics, extenders that amplify human strength and control ability, and upper extremity orthoses. Many exoskeleton designs exist (see, e.g., [1]–[12]), but none have matched or exceeded the capabilities of the human arm in terms of inertia, strength, force-control ability, and range of motion (RoM). To achieve good performance on one or two of these properties typically requires the sacrifice of the good performance on the other properties. For example, strong and light devices have been developed at the cost of using a reduced number of degrees of freedom (DOFs) compared with the human arm [2], [4], [5], [7], [9], [10]. Some higher DOF devices have been designed by the use of electric motors in combination with highly geared mechanisms and force feedback [13]. This gear-reduction factor is typically necessary in order to reduce the power and weight requirements of the electric motors, while achieving the required torque levels; however, such devices typically have large inertia and are costly because they require high-precision-force sensing.

Previous arm exoskeletons have typically used a serial-chain design in which actuators are mounted on progressively more distal serially connected links of the robot. Because of the serial-chain topology, a common strategy to achieve shoulder internal/external rotation [see Fig. 2 (c)] is the use of a serially mounted ring bearing with an actuator that was mounted directly on the ring [1], [3], [14], [15]. This approach fundamentally degrades the force/inertia ratio, which was possible for the arm, because to mount a ring and an actuator on a link that moves increases the overall mass of the mechanism, which the human arm/robotic actuators must carry as they move.
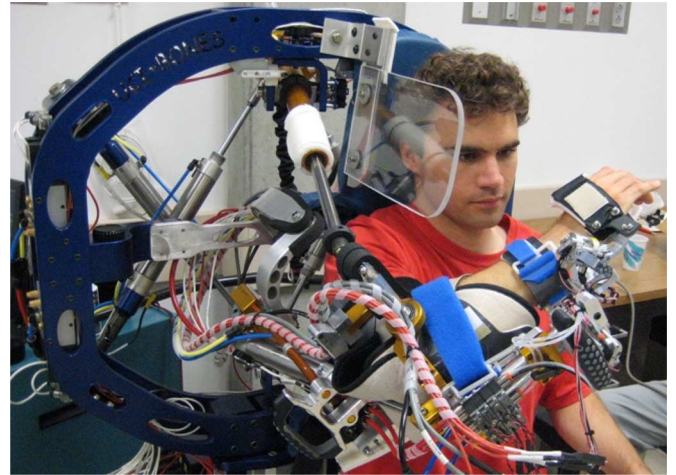
Fig. 1. BONES allows 3-DOF of motion at the shoulder as well as at the elbow flexion/extension. A distal module accommodates forearm supination/pronation and wrist flexion/extension.

In this paper, we present an alternate design strategy that uses a parallel mechanism for the shoulder with mechanically grounded actuators (see Fig. 1). The design for the exoskeleton shoulder was inspired by the design of the human forearm, in which the radius and ulna bones allow forearm rotation without the use of a ring bearing [16]. Use of such a parallel strategy for a robotic device has the advantage that it allows relatively large, direct-drive actuators to be used to generate force, since the weight of the actuators themselves need not be moved. However, the use of a parallel design is a challenge because of the need for a relatively complex mechanism to transmit adequate force through the wide RoM of the human shoulder, while the human arm and body are still accommodated within the mechanism workspace [17]. This paper describes a solution to this problem, which used a design optimization to maximize torque production by the orthosis, while interference with the user's body is avoided.

II. DESIGN DESCRIPTION

The biomimetic orthosis for the neurorehabilitation of the elbow and shoulder (BONES) [18] uses a parallel mechanism, with mechanically grounded actuators, to achieve 3-DOF shoulder movement, which also includes shoulder internal/external rotation (see Fig. 2).

The arm exoskeleton is modeled as an *SR* mechanism, which follows the notation given in [19]: We approximated the shoulder to a spherical joint (S) and the elbow as a revolute joint (R). The spherical shoulder joint was defined by the three intersecting axis, i.e., θ_1, θ_2, and θ_3, as shown in Fig. 3. The main driving mechanism (see Fig. 4) consisted of two *RRPS* linkages: two perpendicular revolute joints (R), followed by a prismatic joint (P), and a spherical joint (S), also according to the notation given in [19]. Similarly, the upper and lower driving linkages constrain the location of the top elbow-connection point (TEC) and the bottom elbow-connection point (BEC), respectively (see Fig. 3). Each driving linkage is actuated by two grounded pneumatic cylinders that form a tetrahedron shape in the backside of BONES (see Fig. 4). (Other actuator types could also be used with this mechanism.) The robot also incorporates a serially placed pneumatic actuator, which was mounted on the upper arm exoskeleton. This actuator is decoupled from the
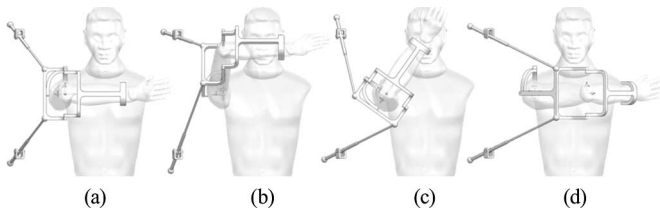
Fig. 2. Several simplified views showing the main driving mechanism and 3 DOF at the shoulder. (a) Arm at rest. (b) Arm elevation θ_1. (c) Internal/external rotation θ_2. (d) Horizontal abduction θ_3.
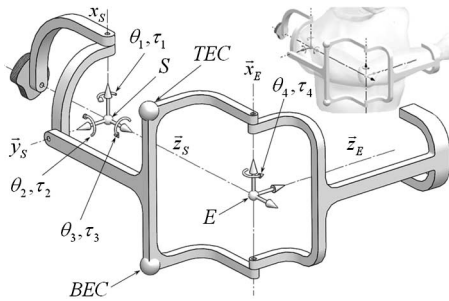

Fig. 3. Original CAD model of the upper arm exoskeleton. S represents the location of the subject's shoulder. E denotes the location of the center of the subject's elbow. TEC is one of the two points through which the upper arm exoskeleton is actuated. BEC is the second point through which the actuation takes place. (Top right) Human model is wearing the exoskeleton.
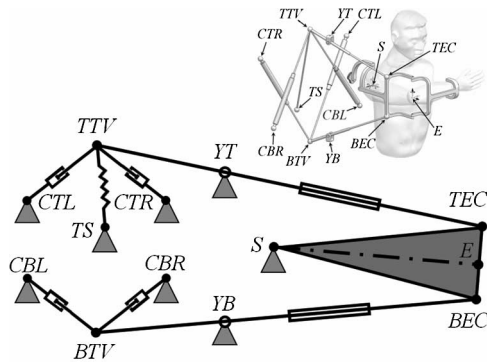

Fig. 4. Shoulder-mechanism actuation diagram. Four cylinders configured in a "diamond structure" drive two bars of changing length, i.e., TTV–TEC and BTV–BEC, respectively. Each bar is hinged by a yoke (YT and YB). A spring attached from TTV to TS provides partial weight support for the arm. (Top right) Schematic solid model of the shoulder mechanism actuation is shown.

shoulder-driving mechanism, and it offers large force output for elbow flexion/extension (θ_4) with light weight.

A single spring-like material, which was implemented by a rubber bungee and attached between the top tetrahedron vertex (TTV) and the main frame at TS (see Fig. 4), provides partial weight support to relieve the mass of a subject's arm and the exoskeleton in any given position, thus resulting in the addition of the essential safety feature that prevents the robot from falling on the subject's lap in the case of an emergency stop or power failure.

A. Key Design Parameters

In the original design for BONES, the main objective was to accommodate a human arm safely: The upper driving bar was located as far away as possible from the subject's head, the lower driving bar was lo-

cated as far away from the rib cage as possible, and the shoulder origin was offset from the center of the robot to better accommodate a patient. TEC and BEC were designed close together, in order to minimize the risk of collision with the subject's lap and head. After the first prototype of BONES was built with design values, which were presented in a conference proceeding [18], we observed that the design had a flaw in that the Jacobian was somewhat ill-conditioned, which causes poor manipulability [20], [21] in certain directions. For example, with the arm in the position shown in Fig. 2(a), the robot was barely strong enough to lift its own weight. For the given pneumatic cylinders and an air pressure of 6.2 bar (90 lb/in^2), the system was not able to generate the desired cylinder forces, due to the fact that in order to move the arm up, i.e., about θ_2, the robot had to provide additional external rotation, i.e., about θ_3, to compensate for the moment arm, which was produced by the forearm against gravity: The Jacobian mapping the forces from cylinder space to the end-effector space was poorly conditioned. Because of the relatively short distance between TEC and BEC, the robot presented a reduced moment arm to generate the required external rotation torque [see Fig. 2(c)]; therefore, substantial actuator force had to be invested to overcome the external rotation, which leaves a reduced amount of force to lift. A possible solution to this problem would have been to increase the maximum force capability for the cylinders with the increase of the cylinder bore and/or the supply air pressure. This solution would have made the robot capable of generating the required torques at the positions with a poorly conditioned Jacobian; however, at the same time, it would have made the robot much stronger in the regions where the Jacobian was already well conditioned, thus making the device undesirably strong and less backdriveable.

In order to make the robot stronger in the critical regions while maintaining the same air supply pressure levels as well as the geometry of the existing pneumatic cylinders, the design itself had to be modified. To assess which design parameters from the original design were the best to modify the torque mapping for the shoulder, we considered several aspects of each of the points, which were described in Fig. 4. First, the mechanical modification had to be simple, with as few operations as possible. Second, the new design had to preserve or improve symmetry in order to allow the robot to be easily reconfigured between left and right arm configuration. Third, the modified parts had to preserve a safe distance between the robot and the patient's body. Finally, the modification had to be reasonably priced.

Taking into account all the previously described aspects, we discarded modification of any of the points, which are located in the "diamond" area [cylinder bottom left (CBL), cylinder bottom right (CBR), cylinder top left (CTL), cylinder top right (CTR), bottom tetrahedron vertex (BTV), and TTV] because of their geometrical complexity. Furthermore, modification of any of these points would lead to having different cylinder strokes (see Fig. 4); therefore, we would have to replace the cylinders and make the redesign costly. Modification of the location of top yoke (YT) and bottom yoke (YB) was also discarded due to the fact that these two points were already designed to provide symmetry and simplify the left/right arm reconfiguration of the robot.

We chose to modify S, TEC, and BEC because of the mechanical simplicity of the joints and the potential to improve the overall symmetry of the robot, while a cost-effective solution is offered.

In order to preserve vertical symmetry, we constrained the coordinates of S to change only in the y-direction (see Fig. 5). We defined p_1 as the distance between the original location of S and the optimal S along the y-axis. To increase the external rotation torque capability, we had to increase the distance between TEC and BEC. At the same time, to maintain safety, we allowed TEC to change only in the positive x-direction, i.e., upward and away from the elbow joint. For the same reason, we constrained BEC to change only in the y-direction,
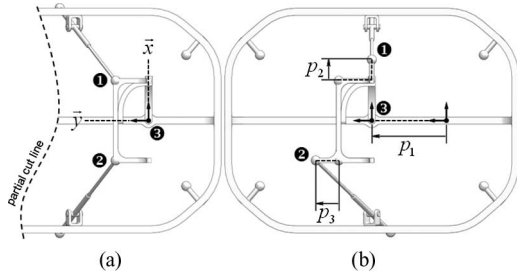
Fig. 5.   Simplified BONES model (a) before optimization and (b) after optimizing. (a) and (b) TEC is labeled as (1), BEC is labeled as (2), and S is labeled as (3). Some components have been hidden for purposes of clarity.

i.e., horizontally and away from the elbow. Furthermore, we decided to vertically align TEC and S to improve the symmetry factor of the optimized design. We defined p_2 as the vertical translation of TEC, and p_3 as the horizontal translation of BEC away from the subject's body. Fig. 5 shows the direction of each parameter's variation and their location before and after the optimization process.

To increase the capability of the robot to lift, it was desirable to reduce the distance between S and the plane that contains YT and YB in order to reduce the additional torque, which was required to balance the arm against gravity. For this reason, p_1 had a significant influence on the capability of the robot to lift the weight of the arm and the exoskeleton. Parameters p_2 and p_3 had a limited effect on the arm-weight-lifting capability, yet both parameters had the potential to fine tune the shape of the force representation and reach our goal.

B. Workspace Representation: Polyhedral Volume

We represented the shoulder-joint-torque capability of the robot at any given arm configuration as a 3-D vector of torques, i.e., τ_1, τ_2, and τ_3, as shown in Fig. 3, which were created by the forces that were generated by the four pneumatic cylinders in the "diamond structure" (see Fig. 4). The force/torque mapping from cylinder coordinates to shoulder joint coordinate was given by

$$\tau = J^T C \qquad (1)$$

where τ is the joint torque vector, C is a 4-D vector of cylinder forces, and J^T is the transpose Jacobian matrix of the mapping for a given configuration [21]. Although there are a total of five pneumatic cylinder that generate four arm torques, i.e., three for the shoulder and one for the elbow, we reduced the overall Jacobian (five actuators mapping onto 4 DOF, $J \in \mathbb{R}^{5 \times 4}$) to a subset $J \in \mathbb{R}^{4 \times 3}$, which maps the four rear actuators to the three shoulder torques. This was possible due to the fact that the elbow actuation is decoupled from the four shoulder actuators. To define the transformation between the four rear actuators and the shoulder torques, we distinguished three intermediate stages. The first stage transformed the velocity vector of the pneumatic cylinders into velocity vectors for TTV and BTV (see Fig. 4). In the second stage, we used the velocity of these two points to determine the velocity of BEC and TEC. Consequently, in the third phase, we transformed the velocities of BEC and TEC into shoulder velocities, i.e., $\dot\theta_1, \dot\theta_2$, and $\dot\theta_3$ from Fig. 3. Detailed derivations for each stage and the full derivation of the Jacobian equations can be found in [22].

The rear "diamond structure" in BONES is composed of four dual-actuated Bimba PFC-175-XBLP cylinders with 3.8 cm (1.5 in) bore and a 14 cm (5.5 in) stroke. With an air-pressure supply of 6.2 bar (90 PSI), each cylinder is capable of generating forces, which range from -628 N ("maximum pull") to $+709$ N ("maximum push"). The force in each cylinder is controlled by two proportional MYPE-5-1/8 LF-010B Festo

valves: one for each cylinder port. The cylinder-force controller was based on [23], which included an experimentally validated mapping of the required valve spool voltage as a function of desired mass-flow rate and chamber pressure. We obtained a level of control, which was comparable with the one described in [23].

Our controller is able to generate forces between "maximum push" and "maximum pull" for each cylinder independently. The set C of all possible cylinder forces is the convex hull of the vertices C_i of the set. These vertices correspond to the points at which each cylinder is working at full capacity in either direction ("maximum push" or "maximum pull"). Because BONES uses four cylinders to create shoulder motion, there are 16 unique C_i, i.e., 16 different combinations of four cylinder forces, which are working at maximum capacity in either direction. Thus, C is defined as follows:

$$C = \sum_{i=1}^{16} C_i w_i \qquad (2)$$

where $\vec{w}$ is a vector such that $\sum_{i=1}^{16} w_i = 1$ and $w_i \geq 0$ [24].

The cylinder force capabilities are independent of one another by assuming an ideal pressure supply. Thus, the set of cylinder forces is convex. The set of torques for a given configuration is the linearly transformed set of forces. Because a linear transformation does not change convexity of a set, the torque space is also convex.

Using (1) into (3), we transform C into the convex hull of all the possible shoulder torques τ, which is defined as follows:

$$\tau = \sum_{i=1}^{16} J^T C_i w_i = \sum_{i=1}^{16} \begin{bmatrix} \tau_{i,1} \\ \tau_{i,2} \\ \tau_{i,3} \end{bmatrix} w_i \qquad (3)$$

where $\vec{w}$ has the same constraints as in (3).

The shape of this polyhedron characterizes the strongest and weakest directions of motion, and it is directly related to the shape of the manipulability ellipsoid [20]. As suggested by Merlet [20], we used the polyhedral representation because it represents a more realistic portrait of our torque-generation capabilities, as compared with the manipulability ellipsoid. A more uniform polyhedral volume indicates that the robot is capable of transitioning from a particular position to another with no preferred direction. In such a situation, the robot has a well-conditioned Jacobian [see (1)]. A narrow polyhedron with an elongated dimension shows a preferred (stronger) direction of motion in that configuration. In such case, the Jacobian is poorly conditioned. It is desirable for a robot to be manipulable, i.e., to be able to move freely with similar effort in any direction, for any given configuration [21].

C. Design Optimization of the Workspace

We started the design-optimization process by determining the value of p_1 that allows BONES to achieve the highest arm-weight-lifting capability without decrease of the safety of the robot: Change in p_1 affected the location of the two driving bars, which potentially bring them closer to the patient, as shown in Fig. 6. We defined our cost function as the average φ^* across a range of arm configurations $\vec\theta_k$

$$\max_{p_1} \frac{1}{n} \sum_{k=1}^{n} \varphi^*(\vec\theta_k, p_1) \quad \text{with } 0 < p_1 < 40 \qquad (4)$$

where φ^* is the maximum weight-lifting torque (about θ_2) that the robot can exert on a subject's arm for a given configuration, and $n = 210$ shoulder configurations were uniformly distributed in the shoulder workspace by $15°$ increments along the RoM, as described in Table II.
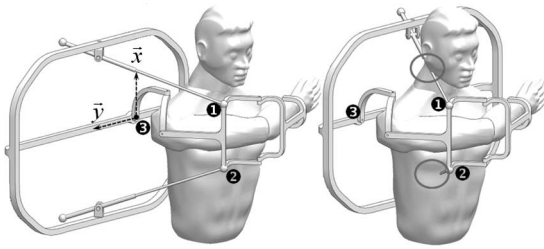
Fig. 6. Moving S too much along the y-axis reduces the safety factor. For some configurations, some parts interfere with the patient's thorax and neck (circled areas, right). TEC is labeled as (1), BEC is labeled as (2), and S is labeled as (3). Some components are hidden for clarity.

We determined the maximum lifting torque at a given configuration $\vec{\theta}_k = (\theta_1, \theta_2, \theta_3)$ and p_1 using

$$\max_w \varphi = \sum_{i=1}^{16} w_i \tau_{i,2}$$

s.t.

$$\sum_{i=1}^{16} w_i \tau_{i,1} = 0$$

$$\sum_{i=1}^{16} w_i \tau_{i,3} = 0$$

$$\sum_{i=1}^{16} w_i = 1$$

$$w_i \geq 0. \tag{5}$$

Equation (6) determines the maximum arm lift (τ_2), while it is ensured that no torques are applied in the other directions. Geometrically, this corresponds to the highest point of the τ_2-axis in the convex hull τ (4). The convexity of the set guaranteed a unique solution for φ given $\vec{\theta}_k$ and p_1 [24]. Equation (6) was in the form of a linear-programming-optimization problem. We solved it by the use of *linprog*, i.e., a linear problem solver, which was included in the optimization toolbox in MATLAB [25]. We set *linprog* to choose an initial condition automatically and return the maximized value $\phi^*(\vec{\theta}_k, p_1)$. This suboptimization was solved at each iteration of (5).

To solve (5), we used the constrained nonlinear multivariable function solver *fmincon*, which is also included in the optimization toolbox in MATLAB. Given a set of initial conditions, the solver attempts to find a minimizer p_1 for (5), subject to a set of lower and upper bounds on the design variable: $0 \text{ cm} \leq p_1 \leq 40 \text{ cm}$. This bound corresponded to the maximum range in the structural frame along which we could potentially move S [in the direction of the positive y-axis in Fig. 5 (a)]. Additionally, this bound served as a safety measure because translating S to far away from the sagittal plane would bring the driving bars (YT–TEC and BY–BEC; see Fig. 4) closer to the patient's head and torso (see Fig. 6). In addition, we set the minimum change in the optimization variable for finite-difference gradients to 0.01 cm in order to match the tolerance of our fabrication process. The initial condition was set to $p_1 = 0.00$ cm, which corresponds to the location of S before the optimization process [see Fig. 5 (a)].

According to [26], the human arm generates levels of torque as high as 10 N·m for typical activities of daily living (ADL). In order to verify that BONES could excel past this 10 N·m threshold, we plotted the results of (5) as a ratio between φ^* and 22 N·m (10 N·m
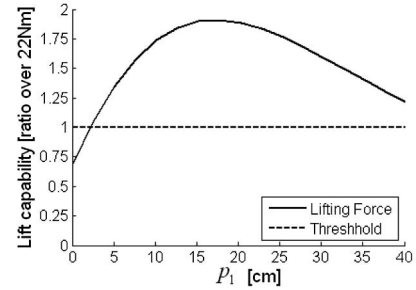

Fig. 7. Optimization of the arm-weight-lifting capability, which is expressed as a ratio over 22 N·m, as a function of p_1. The optimal value appears at $p_1 = 17.12$ cm, with a corresponding maximal ratio of 1.89 (89% exceeding over the 22 N·m threshold).
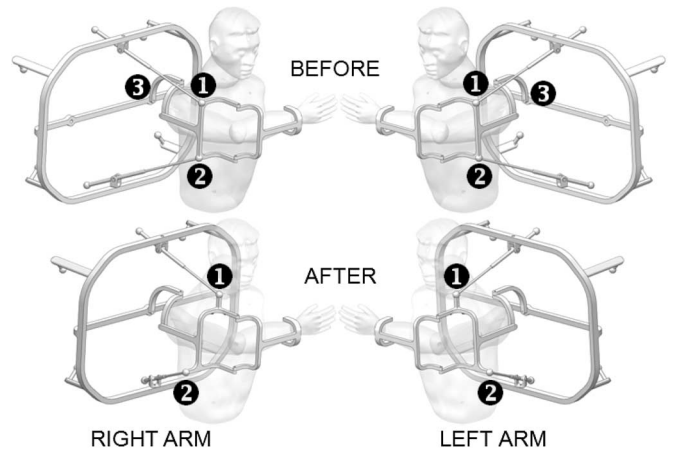

Fig. 8. Comparison between the design in left and right arm configuration, before and after the optimization method. Labels indicated the number of parts that need to be disassembled in order to configure the robot from right to left arm or *vice versa*. In both designs, during the reconfiguration process, the sliding bars need to be disengaged from TEC and BEC, which are labeled as 1 and 2, respectively. In the original design, an additional third part, which is labeled as 3, needed to be disassembled for the reconfiguration process.

for the arm plus 12 N·m to lift the weight of the exoskeleton). The arm-lifting ratio as a function of p_1 is shown in Fig. 7. Although the results of the optimization method would encourage to set p_1, which correspond to the highest ratio ($p_1 = 17.12$ cm, ratio = 1.89), we took into consideration the benefits of preserving symmetry, as previously described. By offsetting p_1 to 20.32 cm (8 in), we translated the shoulder to the sagittal symmetry plane of the supporting frame. If the robot had to be reconfigured from left to right arm configuration, any point that was located on the sagittal plane would remain in the same location; therefore, it reduces the number of parts that need reassembly during the reconfiguration process. Fig. 8 shows the original design and the optimized one for the left and right arm configuration. In the optimized design, we reduced the number of parts that need to be reassembled from three to two.

Before the optimization, the robot was not able to generate 22 N·m for some directions; therefore, the required torque space sphere was partially exposed. After optimization, the robot exceeded 22 N·m in all directions and the sphere was fully covered by the convex hull (see Fig. 9).

After the optimal value for p_1 was determined, we continued the optimization process with p_2 and p_3. For these two parameters, our goal was to optimize the ratio between the shortest and the longest axis of the polyhedral volume in order to discourage any undesirable
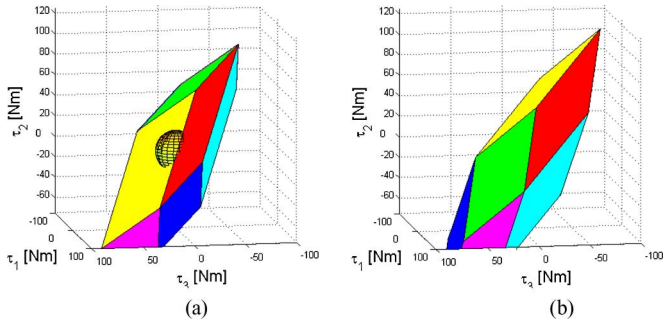
Fig. 9.   Shoulder-joint torque capacity represented by a polyhedral volume. (a) For some specific direction, the originally designed robot cannot achieve 22 N·m, represented by a sphere. (b) After adjusting three design parameters, the robot exceeds 22 N·m in all directions with the arm in the home position.

Fig. 10.   Optimization of the conditioning ratio as a function of p_2 and p_3. The optimal value appears at $p_2 = 5.72$ cm (2.25 in) and $p_3 = 7.62$ cm (3 in), with a corresponding conditioning ratio of 0.53.

TABLE I
TORQUES APPLIED BY OR TO THE ARM [IN N·m]

	BONES[1]	BONES[2]	Paretic Arm[3]	Nonparetic Arm[4]	ADL
τ_1	83.0	76.8	27.2	53.9	8.0
τ_2	39.0	50.0	41.2	53.5	10.0
τ_3	28.0	42.2	19.1	35.6	1.0
τ_4	68.0	68.0	38.7	80.9	3.5

1---Maximum values for the configuration shown in Fig. 3, before optimization, 2---maximum values for the same configuration, after optimization, 3---typical maximal voluntary torques for a stroke survivor's paretic arm, according to [29], and 4---maximal voluntary torques for an unimpaired human arm, according to [29]. Typical ADL torque values applied by the arm, extracted from [28].

TABLE II
RoM OF BONES [30]

	BONES[1] (min/max)	BONES[2] (min/max)	BONES[1] RoM	BONES[2] RoM	ADL RoM
θ_1	-45/60	-49/50	105	99	110
θ_2	-35/45	-33/40	80	73	100
θ_3	5/60	5/81	55	76	135
θ_4	12/84	12/84	68	68	150

1---Before optimization and 2---after optimization. Angles are measured with respect to the position shown in Fig. 3. ADL RoM obtained from [28].

direction to be stronger than the rest. By making the major axis and the minor axis similar, we were reshaping an ellipsoid-like volume into a sphere, therefore, equalizing the maximal applicable strength for any given direction. This ratio is related to the condition of the Jacobian matrix and the manipulability of the robot [20], [21]. When a Jacobian matrix is poorly conditioned in a given direction, the singular value, which corresponds to the vector in that direction, is small in comparison with the other singular values of the Jacobian. The poorly conditioned singular value will cause difficulties in the numerical calculation along that direction, as if we were approaching a singular point [20], [27]. The forces along the vector, which is associated with that singular value, will be very low, as compared with better conditioned directions, i.e., with lower condition numbers. Therefore, it is desirable that the Jacobian matrix remains as well conditioned as possible, with condition numbers as low as possible in all directions. A well-conditioned Jacobian will translate directly into a system, which is capable of generating similar forces in all directions.

The optimization function that we used to maximize the manipulability of the robot was

$$\max_{p_2, p_3} \frac{1}{n} \sum_{k=1}^{n} \frac{1}{cond(J(\vec{\theta}_k, p_2, p_3))}$$

$$\text{with } 0 < p_2 < 10$$

$$\text{and } 0 < p_3 < 10 \qquad (6)$$

where *cond* is a function that determines the condition of the Jacobian matrix in terms of $\vec{\theta}_k$, p_2, and p_3. Prior to the optimization process, an initial brute force sweep across the mapping estimated the existence of local minima/maxima. This initial sweep was calculated for -20 cm $\leq p_2 \leq 20$ cm and -20 cm $\leq p_3 \leq 20$ cm, but during the optimization process, the variable boundaries were set to 0 cm $\leq p_2 \leq 10$ cm and 0 cm $\leq p_3 \leq 10$ cm due to the mechanical restrictions in the original design and to discard solutions, which lead to undesirably large parts that would reduce the overall safety of the design. Initial conditions were set to $p_2 = 0.00$ cm and $p_3 = 0.00$ cm. We used the same minimum step size of 10^{-2} cm, as described previously. The condition as a function of p_2 and p_3 is shown in Fig. 10.

After implementation of the optimized hardware modifications, the performance of BONES improved substantially. First, the arm-weight-lifting capabilities, which were measured as the average vertical force with respect to arm weight across the entire workspace, increased from 63% to 189% of typical human-arm weight. Second, the torque distribution has presented a more homogeneous scenario, which decreases the dominance of τ_1 and, consequently, reduces the undesirable exis-
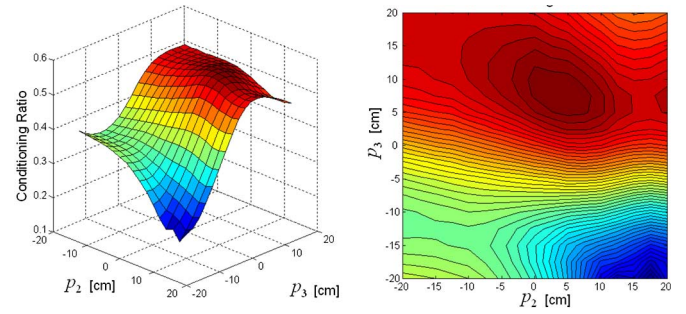
tence of a preferred direction of motion (see Table I). Additionally, the optimization improved the external rotation RoM by 25%, with respect to the original design. The other DOF did not change significantly (see Table II). The RoM of BONES accommodates most rehabilitation activities that were involved in ADL. Although the range of elbow flexion (θ_4) in BONES covers only about 50% of the typical range, which was suggested by Perry *et al.* [28], we designed the elbow mechanism to provide full elbow extension, while the maximum elbow flexion was limited to 90°. Similarly, for internal/external rotation [θ_3, Fig. 2(c)], we limited the rotation mechanism that prevents it from internally rotating the arm (negative rotation about θ_3) below the configuration, which was shown in Fig. 2(a), in order to prevent shoulder pain. The range of external rotation with BONES is adequate for ADL exercises that involve this movement.

The shoulder mechanism, before and after the optimization process, is shown in Fig. 8, where the right and the left arm configurations are compared, and the number of parts that were required to reconfigure the robot are labeled.

III.   CONCLUSION

This paper has presented the design and kinematic optimization procedure for BONES: a novel robot that allows naturalistic motion of the human arm with the use of mechanically grounded, direct-drive actuators at the shoulder. Direct-drive actuation is achieved with a relatively

simple mechanism, which was inspired by the human forearm. The optimization procedure presented here shows that the force-generating capacity of this mechanism is very sensitive to its kinematic parameters. However, following the optimization technique described here, the mechanism's RoM, inertia, and force-generating capacity match well with the human arm.

Since April 2009, we have been using BONES in a rehabilitation clinic to retrain arm-movement ability after stroke, with the use of the adaptive control algorithms that were described in [31]. BONES is allowing us to rigorously test whether functional transfer of robotic therapy is improved with the practice of naturalistic arm movements.

REFERENCES

[1] M. Bergamasco, B. Allotta, L. Bosio, L. Ferretti, G. Parrini, G. M. Prisco, F. Salsedo, and G. Sartini, "An arm exoskeleton system for teleoperation and virtual environments applications," in *Proc. IEEE Int. Conf. Robot. Autom.*, 1994, vol. 2, pp. 1449–1454.

[2] S. Coote, E. K. Stokes, B. T. Murphy, and W. S. Harwin, "The effect of GENTLE/s robot mediated therapy on upper extremity function post stroke," in *Proc. Int. Conf. Rehabil. Robot.*, 2003, pp. 59–61.

[3] A. Frisoli, F. Rocchi, S. Marcheschi, A. Dettori, F. Salsedo, and M. Bergamasco, "A new force-feedback arm exoskeleton for haptic interaction in virtual environments," in *Proc. First Joint Eurohaptics Conf. Symp. Haptic Interfaces Virtual Environ. Teleoperator Syst.*, 2005, pp. 195–201.

[4] S. Hesse, C. Werner, M. Pohl, S. Rueckriem, J. Mehrholz, and M. L. Lingnau, "Computerized arm training improves the motor control of the severely affected arm after stroke: A single-blinded randomized trial in two centers," *Stroke*, vol. 36, pp. 1960–1966, Sep. 2005.

[5] N. Hogan, H. Krebs, A. Sharon, and J. Charnnarong, *Interactive Robot Therapist*. Cambridge, MA: MIT Press, 1995.

[6] Y. Hurmuzlu, A. Ephanov, and D. Stoianovici, "Effect of a pneumatically driven haptic interface on the perceptional capabilities of human operators," *Presence: Teleoperators Virtual Environ.*, vol. 7, pp. 290–307, Jun. 15, 1998.

[7] L. Kahn, M. Zygman, W. Z. Rymer, and D. Reinkensmeyer, "Robot-assisted reaching exercise promotes arm movement recovery in chronic hemiparetic stroke: A randomized controlled pilot study," *J. NeuroEng. Rehabil.*, vol. 3, p. 12, 2006.

[8] T. Nef, M. Mihelj, G. Kiefer, C. Perndl, R. Muller, and R. Riener, "ARMin—Exoskeleton for arm therapy in stroke patients," in *Proc. IEEE 10th Int. Conf. Rehabil. Robot.*, 2007, pp. 68–74.

[9] D. J. Reinkensmeyer, L. E. Kahn, M. Averbuch, A. McKenna-Cole, B. D. Schmit, and W. Z. Rymer, "Understanding and treating arm movement impairment after chronic brain injury: Progress with the ARM guide," *J. Rehabil. Res. Dev.*, vol. 37, pp. 653–662, Nov. 2000.

[10] R. Riener, T. Nef, and G. Colombo, "Robot-aided neurorehabilitation of the upper extremities," *Med. Biol. Eng. Comput.*, vol. 43, pp. 2–10, Jan. 2005.

[11] R. J. Sanchez, E. T. Wolbrecht, R. Smith, J. Liu, S. Rao, S. Cramer, T. Rahman, J. E. Bobrow, and D. J. Reinkensmeyer, "A pneumatic robot for re-training arm movement after stroke: Rationale and mechanical design," in *Proc. 9th Int. Conf. Rehabil. Robot.*, 2005, pp. 500–504.

[12] T. G. Sugar, H. Jiping, E. J. Koeneman, J. B. Koeneman, R. Herman, H. Huang, R. S. Schultz, D. E. Herring, J. Wanberg, S. Balasubramanian, P. Swenson, and J. A. Ward, "Design and control of RUPERT: A device for robotic upper extremity repetitive therapy," *IEEE Trans Neural Syst Rehabil Eng.*, vol. 15, no. 3, pp. 336–346, Sep. 2007.

[13] M. Mihelj, T. Nef, and R. Riener, "ARMin II—7 DoF rehabilitation robot: Mechanics and kinematics," in *Proc. IEEE Int. Conf. Robot. Autom.*, 2007, pp. 4120–4125.

[14] C. Carignan, M. Liszka, and S. Roderick, "Design of an arm exoskeleton with scapula motion for shoulder rehabilitation," in *Proc. 12th Int. Conf. Adv. Robot.*, 2005, pp. 524–531.

[15] L. Q. Zhang, H. S. Park, and Y. Ren, "Developing an intelligent robotic arm for stroke rehabilitation," in *Proc. IEEE 10th Int. Conf. Rehabil. Robot.*, 2007, pp. 984–993.

[16] A. Kecskeméthy and A. Weinberg, "An improved elasto-kinematic model of the human forearm for biofidelic medical diagnosis," *Multibody Syst. Dyn.*, vol. 14, pp. 1–21, 2005.

[17] B. D. Adelstein, "Three degree of freedom parallel mechanical linkage," U.S. Patent 5 816 105, Oct. 6, 1998.

[18] J. Klein, S. J. Spencer, J. Allington, K. Minakata, W. Wolbrecht, R. F. Smith, J. Bobrow, and D. J. Reinkensmeyer, "Biomimetic orthosis for the neurorehabilitation of the elbow and shoulder (BONES)," in *Proc. BioRob*, Scottsdale, AZ, 2008, pp. 535–541.

[19] J. M. McCarthy, *Geometric Design of Linkages (Interdisciplinary Applied Mathematics)*, 1st ed. New York: Springer-Verlag, 2000.

[20] J. P. Merlet, "Jacobian, manipulability, condition number, and accuracy of parallel robots," *J. Mech. Des.*, vol. 128, pp. 199–206, 2006.

[21] R. Murray, Z. Li, and S. Sastry, *A Mathematical Introduction to Robotic Manipulation*. Boca Raton, FL: CRC, 1994.

[22] J. Klein, "Performance enhancing mechanisms for human manipulation," Ph.D. dissertation, Dept. Mech. Aerospace Eng., Univ. Calif., Irvine, 2009.

[23] E. T. Wolbrecht, D. J. Reinkensmeyer, and J. E. Bobrow, "Pneumatic control of robots for rehabilitation," *Int. J. Robot. Res.*, vol. 29, pp. 23–38, 2010.

[24] R. Fletcher, *Practical Methods of Optimization*, 2nd ed. New York: Wiley, 2000.

[25] Mathworks, *MATLAB* R2009A ed., 2009.

[26] J. Rosen, J. C. Perry, N. Manning, S. Burns, and B. Hannaford, "The human arm kinematics and dynamics during daily activities—Toward a 7 DOF upper limb powered exoskeleton," in *Proc. 12th Int. Conf. Adv. Robot.*, 2005, pp. 532–539.

[27] Y. Saad, "Numerical solution of large nonsymmetric eigenvalue problems," *Comput. Phys. Commun.*, vol. 53, pp. 71–90, 1989.

[28] J. C. Perry, J. Rosen, and S. Burns, "Upper-limb powered exoskeleton design," *IEEE/ASME Trans. Mechatronics*, vol. 12, no. 4, pp. 408–417, Aug. 2007.

[29] J. P. A. Dewald and R. F. Beer, "Abnormal joint torque patterns in the paretic upper limb of subjects with hemiparesis," *Muscle Nerve*, vol. 24, pp. 273–283, 2001.

[30] C. A. Hautier, L. M. Arsac, K. Deghdegh, J. Souquet, A. Belli, and J.-R. Lacour, "Influence of fatigue on EMG/force ratio and cocontraction in cycling," *Med. Sci. Sports Exerc.*, vol. 32, pp. 839–843, 2000.

[31] E. Wolbrecht, "Adaptive, assist-as-needed control of a pneumatic orthosis for optimizing robotic movement therapy following stroke," Ph.D. dissertation, Dept. Mech. Aerospace Eng., Univ. Calif., Irvine, 2007.

Detecting Region Transitions for Human-Augmented Mapping

Elin A. Topp and Henrik I. Christensen

Abstract—In this paper, we describe a concise method for the feature-based representation of *regions* in an indoor environment and show how it can also be applied for door-passage-independent detection of transitions between *regions* to improve communication with a human user.

Index Terms—Human–robot interface, semantic mapping, space segmentation.

I. INTRODUCTION

In this paper, we aim to develop a case for a concise method for the segmentation of an indoor environment into a topological-graph

E. A. Topp was with the Centre for Autonomous Systems, Royal Institute of Technology (KTH), Stockholm 10044, Sweden. She is now with the Department of Computer Science, Lund University (LTH), Lund 22100, Sweden (e-mail: elin_anna.topp@cs.lth.se).

H. I. Christensen is with the College of Computing, Georgia Institute of Technology, Atlanta, GA 30332-0760 USA (e-mail: hic@cc.gatech.edu).